Nonlinear Wave-Packet Interferometry and Molecular State Reconstruction in a Vibrating and Rotating Diatomic Molecule†

Travis S. Humble‡ and Jeffrey A. Cina*

Department of Chemistry and Oregon Center for Optics, University of Oregon, Eugene, Oregon 97403-1253

Received: November 22, 2005

We formulate two-color nonlinear wave-packet interferometry (WPI) for application to a diatomic molecule in the gas phase and show that this form of heterodyne-detected multidimensional electronic spectroscopy will permit the reconstruction of photoinduced rovibrational wave packets from experimental data. Using two phase-locked pulse pairs, each resonant with a different electronic transition, nonlinear WPI detects the quadrilinear interference contributions to the population of an excited electronic state. Combining measurements taken with different phase-locking angles isolates various quadrilinear interference terms. One such term gives the complex overlap between a propagated one-pulse target wave packet and a variable three-pulse reference wave packet. The two-dimensional interferogram in the time domain specifies the complex-valued overlap of the given target state with a collection of variable reference states. An inversion procedure based on singular-value decomposition enables reconstruction of the target wave packet from the interferogram without prior detailed characterization of the nuclear Hamiltonian under which the target propagates. With numerically calculated nonlinear WPI signals subject to Gaussian noise, we demonstrate the reconstruction of a rovibrational wave packet launched from the A state and propagated in the E state of Li_2.

I. Introduction

Time-resolved phase-coherent multidimensional electronic spectroscopy (MDES) is a powerful tool for understanding chemical processes. Using phase-stabilized sequences of femtosecond laser pulses resonant with molecular electronic transitions, this form of nonlinear optical spectroscopy[1,2] probes ultrafast chemical dynamics at the level of coherent response functions and quantum-mechanical amplitudes (wave functions) rather than their squares (probability densities). In analogy with multidimensional nuclear magnetic resonance (NMR) techniques, MDES prepares electronic, vibrational, and rotational populations and coherences and monitors their subsequent time development.[3−6] In contrast with the nanosecond time scale of NMR, the femtosecond-duration pulses of MDES monitor the nonlinear optical response as the molecular state evolves on the fundamental time scale of chemical change.[7]

As an example of MDES, two-dimensional Fourier transform electronic spectroscopy excites a third-order nonlinear polarization using a sequence of three noncollinear pulses.[8] A fourth pulse overlapped with the subsequently emitted electric field allows heterodyne detection of the nonlinear polarization; by stabilization of the phases among incident pulses, the real and imaginary components of the molecular response can be measured.[1,9,10] A collection of these measurements, performed as a function of the interpulse delays, is typically Fourier transformed to obtain a frequency-domain representation of the nonlinear optical response.[8,11,12] Recent experiments have implemented phase-coherent MDES techniques to provide detailed pictures of the spatial and energetic dynamics in complex molecular systems.[13−15]

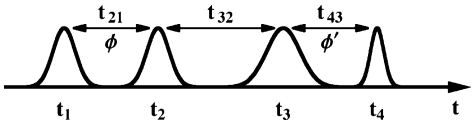

Figure 1. Sequence of two phase-locked pulse pairs used in two-color nonlinear WPI. The pulses arrive in sequence, $t_1 < t_2 < t_3 < t_4$, and pulse overlap is neglected. Pulses 1 and 2 have a common carrier frequency $\Omega_1 = \Omega_2$ and an intrapulse-pair optical phase shift $\phi = \phi_2(\omega_L) - \phi_1(\omega_L) - \omega_L t_{21}$. Pulses 3 and 4 have frequency $\Omega_3 = \Omega_4$ and phase shift $\phi' = \phi_4(\omega'_L) - \phi_3(\omega'_L) - \omega'_L t_{43}$. The delay t_{43} is the same for all measurements, while t_{21} and t_{32} are varied.

There are additional capabilities in nonlinear optical spectroscopy without widely employed analogies in NMR. As noted earlier, femtosecond-duration pulses allow rovibronic populations and coherences of an excited system to be time resolved. For a molecular system, electronic excitation by a broadbandwidth pulse prepares time-dependent nuclear states. Thus the molecule's response reflects quantum-mechanical interference among the nuclear wave packets prepared by the pulse sequence and propagated under the relevant nuclear Hamiltonians. The excited populations and coherences of nuclear spin states are not usually of immediate chemical significance, and their explicit determination is not a typical objective of NMR experiments. From a chemical viewpoint, the nuclear dynamics set in motion by short-pulse electronic excitation and monitored by MDES is directly pertinent to the microscopic understanding of photochemical reactions.

Here we formulate two-color nonlinear wave packet interferometry (WPI) as an application of MDES employing a sequence of two phase-locked pulse pairs (see Figure 1). Using a wave packet description of the nonlinear optical response, we show that with optical phase control and spectral selection it is possible to disentangle the multiple interferences of pulse-induced nuclear wave packets contributing to a measured

* To whom correspondence may be addressed. E-mail: cina@uoregon.edu.
† Part of the special issue "Robert J. Silbey Festschrift".
‡ Present address: Oak Ridge National Lab, Building 5600, MS-6016, Oak Ridge, TN 37831-6016.

10.1021/jp0567669 CCC: $33.50 © xxxx American Chemical Society
Published on Web 04/18/2006 PAGE EST: 13.1

electronic-state population. We further demonstrate that the nonlinear WPI signal provides sufficient amplitude-level information to reconstruct a time-dependent target wave packet propagated under the perhaps ill-characterized nuclear Hamiltonian of that excited electronic state.

State reconstruction has served as an organizing concept in the field of quantum optics[16] and could also be of considerable value for illuminating photochemical reaction dynamics at the most basic level. For instance, our formulation of molecular state reconstruction could serve as a diagnostic complement to closed-loop feedback-controlled pulse-shaping techniques.[17−20] Guided by learning algorithms, those methods search for the spectral amplitudes and phases that shape a broadband pulse so as to most effectively initiate a targeted molecular response.[21] As experiments of this kind are often carried out on systems whose Hamiltonian is not well-known,[22,23] a method to reconstruct photoinduced states with imperfect knowledge of the Hamiltonian could provide insight into the quantum dynamics mediating preparation of the targeted molecular state, which would otherwise be lacking.

Several groups have used wave packet interferometry to characterize atomic and molecular wave packets.[24−34] In the original linear WPI experiments, a single pair of time-delayed phase-locked pulses excited a superposition of nuclear wave packets in the B electronic level of gas-phase I_2.[24,25] In an optical analogy with Young's double-slit experiment,[26] Scherer et al. showed that by measuring the portion of the B-state population bilinear in the laser fields as a function of intrapulse-pair delay and phase shift, the complex-valued overlap of the two "one-pulse" nuclear wave packets could be followed in time.[24] The first of these one-pulse packets, here termed the target state, propagates on the B-state potential for the intrapulse-pair delay, while the second wave packet, termed the reference state, remains in the X state and is transferred to the B state by the second pulse. In the short-pulse limit, their bilinear interference directly reveals the time-dependent kernel familiar from Heller's formulation of linear absorption.[25,35]

Girard and co-workers applied linear WPI to gain temporal coherent control over the population of both atomic[27−29] and diatomic[30] electronic levels, while Ohmori et al. took a similar approach in controlling the population dynamics of a van der Waals complex.[31] Gühr et al. used linear WPI to monitor and control vibrational decoherence of diatomic halides trapped in rare gas matrixes.[32] In another condensed phase application, Milota et al. investigated homogeneous dephasing processes in conjugated polymers by measuring fluorescence interference.[33] Martínez-Galicia and Romero-Rochín explored linear WPI from the viewpoint of the incident fields, which, in a quantum mechanical analysis, become entangled with the excited molecular system.[34]

Leichtle et al. have shown how measurements of the bilinear interference can characterize a shaped vibrational wave packet using quantum state holography (QSH).[36] In this application of linear WPI, the target state is prepared by the first (possibly shaped) pulse and propagation under the excited-state Hamiltonian, while the reference state is created by the time-delayed second pulse and an interval of forward or backward propagation on the same presumably well-known excited-state potential. With measurements of the wave packet interference as a function of intrapulse-pair delay and phase-locking angle along with knowledge of the prepared reference states, QSH expresses the interferogram as a set of linear algebraic equations that can be numerically inverted to yield expansion coefficients for the target state in a basis of nuclear eigenfunctions of the excited electronic state. Experimentally, Bucksbaum and co-workers have implemented QSH to reconstruct electronic Rydberg wave packets in cesium atoms and to guide the shaping of quantum states with closed-loop feedback control.[37]

Our approach to state reconstruction via nonlinear WPI has some features in common with QSH but aspires to extend wave packet reconstruction to situations where the relevant excited-state Hamiltonian is unknown, or at best ill-characterized. In nonlinear WPI,[38−45] one detects the interference contributions to an excited-state population generated by *two* pairs of phase-locked pulses. The quadrilinear contribution to the excited-state population—that portion linear in all four applied fields—arises from quantum-mechanical interference between various one-pulse and three-pulse wave packets. As shown in previous studies of one-color nonlinear WPI,[39−41] in which both pulse pairs drive the same electronic transition, there are four overlaps contributing to the quadrilinear interference, which can be grouped according to their dependence on the optical phase shifts: two overlaps depend on the sum of the phase-locking angles, while the other two depend on the difference. Shifting the phase-locking angles allows the phases of the two types of terms to be changed independently; by combining WPI measurements with different phase-locking angles, the two sums can be experimentally isolated. Although certain dynamical features (such as a dissociative potential surface or multiple incommensurable mode frequencies) can minimize the simultaneous occurrence of overlaps with the same phase signature, individual quadrilinear overlaps are not isolable in general in one-color nonlinear WPI experiments.[39−41] A more fundamental limitation is the fact that—as with QSH—wave packet reconstruction based on one-color WPI data requires quantitative characterization of the common excited-state nuclear Hamiltonian under which both the target and reference states propagate.

The situation is different in two-color nonlinear WPI,[39,43,45] where the first pulse pair drives transitions between the initial and intermediate electronic levels, while the second pulse pair drives transitions between the initial and final levels. In this situation, the final-state population contains only two quadrilinear overlaps—each with a different phase signature—and these two overlaps can be separately isolated. The one taking the form of an overlap between a one-pulse target state that propagates under the unknown final-state nuclear Hamiltonian and a three-pulse reference state that propagates only in the well-characterized potentials of the initial and intermediate electronic levels provides the necessary information for reconstruction of the sought-after target state.

We recently examined one- and two-color nonlinear WPI for bound[43] and photodissociative[45] model systems supporting a single, vibrational, degree of freedom. We explored reconstruction of target states shaped by chirped pulses from calculated nonlinear WPI signals and investigated the effects of both signal noise and finite temperature. In this paper, we continue our investigation of two-color nonlinear WPI for the reconstruction of optically prepared nuclear wave packets by performing rigorous numerical calculations on a three-dimensional molecular system, namely, a vibrating and rotating diatomic molecule in the gas phase. We chose the lithium dimer for this study, in part because accurate ab initio potentials and transition dipole moments are available for several electronic levels.[46] In addition, Li_2 has been the subject of recent coherent-control experiments by Leone and co-workers,[47−51] who monitored the dynamics of rovibrational wave packets in the E state of Li_2 by pump−probe photoionization spectroscopy and demonstrated control over their time evolution with shaped optical pulses. These

features suggest that the lithium dimer is a suitable test bed for theoretical and experimental studies of two-color nonlinear WPI and molecular state reconstruction.

Section II outlines the basic theory of two-color nonlinear WPI and shows how optical phase shifting can be used to isolate the quantum-mechanical overlaps needed for molecular state reconstruction. Section III explains our state reconstruction technique, and section IV specializes the theoretical treatment to the case of a rotating diatomic molecule. State determination for Li_2 is carried out in section V using numerically calculated interference signals. We determine the extent to which state reconstruction can be successfully effected despite a lack of quantitative knowledge of the final-state potential and transition dipole moment. In section VI we discuss our findings and the correspondence between nonlinear WPI and other forms of MDES. We conclude by commenting on the prospects for future applications of nonlinear WPI.

II. Two-Color Nonlinear WPI

The field-free Hamiltonian of the molecule is

$$H = |g\rangle H_g \langle g| + |e\rangle H_e \langle e| + |f\rangle H_f \langle f|, \tag{1}$$

where H_g, H_e, and H_f are the nuclear Hamiltonians of the ground, intermediate, and final electronic states, $|g\rangle$, $|e\rangle$, and $|f\rangle$, respectively. Our reconstruction scheme requires that H_g and H_e be well characterized but does not assume such information for H_f (which governs the time evolution of the target state). This situation may occur when g and e are low-lying electronic levels accessible to experimental or computational characterization and f is a higher-lying, less easily characterized electronic level.

In the proposed experiment, the system evolves under the time-dependent Hamiltonian $H(t) = H + V(t)$. The interaction between the molecule and two pairs of phase-locked pulses is written as

$$V(t) = \sum_{j=1}^{4} V_j(t) \tag{2}$$

where

$$V_j(t) = -\hat{\boldsymbol{\mu}} \cdot \mathbf{E}_j(t) \tag{3}$$

The dipole moment operator

$$\hat{\boldsymbol{\mu}} = \boldsymbol{\mu}_{fg}|f\rangle\langle g| + \boldsymbol{\mu}_{eg}|e\rangle\langle g| + \boldsymbol{\mu}_{fe}|f\rangle\langle e| + H.c. \tag{4}$$

couples electronic levels a and b through the nuclear-coordinate-dependent transition dipole moment vector $\boldsymbol{\mu}_{ba}$. *H.c.* stands for Hermitian conjugate. The jth electric field

$$\mathbf{E}_j(t) = \mathbf{e}_j A_j(t - t_j) \cos \Phi_j(t - t_j) \tag{5}$$

has arrival time t_j, linear polarization vector $\mathbf{e}_j$, envelope function $A_j(t)$, and temporal phase $\Phi_j(t)$. We assume that the pulses arrive in sequence, $t_1 < t_2 < t_3 < t_4$, and do not overlap in time; the delay between pulses j and k is $t_{jk} = t_j - t_k$. The first and second pulses constitute one phase-locked pulse pair, and the third and fourth pulses constitute a second. The first pulse pair drives the e $\leftrightarrow$ g electronic transition, and the second pulse pair drives the f $\leftrightarrow$ g transition. Neither pair is resonant with f $\leftrightarrow$ e. In our state determination scheme, the intrapulse-pair delay t_{43} is held constant, as this interval specifies the f-state propagation time of a target wave packet. The remaining time delays, t_{21} and t_{32}, are varied and specify the members of a family of reference wave packets.

Phase locking each pulse pair fixes the relative spectral phase of the two pulses at a selected locking frequency. The Fourier component of the jth pulse at frequency ω is

$$\begin{aligned}\alpha_j(\omega) e^{-i\phi_j(\omega) + i\omega t_j} &= \int_{-\infty}^{\infty} dt e^{i\omega t} A_j(t - t_j) \cos \Phi_j(t - t_j) \\ &\cong \frac{e^{i\omega t_j}}{2} \int_{-\infty}^{\infty} dt e^{i\omega t} A_j(t) e^{-i\Phi_j(t)}\end{aligned} \tag{6}$$

where $\alpha_j(\omega)$ and $\phi_j(\omega) - \omega t_j$ are the spectral amplitude and phase, respectively. In the last line of eq 6, we make the slowly varying envelope approximation by assuming that the pulse duration, though perhaps abrupt compared to nuclear motion, is many times an optical period (and $\Phi_j(t)$ is defined to increase monotonically). Phase locking the first pulse pair at the locking frequency ω_L requires that the optical phase shift

$$\phi = \phi_2(\omega_L) - \phi_1(\omega_L) - \omega_L t_{21} \tag{7}$$

be held constant as the intrapair delay t_{21} is scanned. Phase locking the second pulse pair at ω'_L similarly specifies a phase shift

$$\phi' = \phi_4(\omega'_L) - \phi_3(\omega'_L) - \omega'_L t_{43} \tag{8}$$

We solve for the amplitude of the molecular state using time-dependent perturbation theory, and truncate the expansion at third order in the incident fields because higher terms are presumed negligible or would not contribute to the fourth-order f-state population. The molecular state before the arrival of the pulses is

$$|\Psi(t \ll t_1)\rangle = |g\rangle e^{-iH_g(t - t_3)} |n_g\rangle \tag{9}$$

where $|n_g\rangle$ is an eigenstate of H_g with energy $E_g(n_g)$, and we set $\hbar = 1$. To follow the time evolution, we switch to the interaction picture

$$|\tilde{\Psi}(t)\rangle = e^{iH(t - t_3)} |\Psi(t)\rangle \tag{10}$$

and solve the corresponding equation of motion

$$i \frac{\partial |\tilde{\Psi}(t)\rangle}{\partial t} = \tilde{V}(t) |\tilde{\Psi}(t)\rangle \tag{11}$$

for the state-ket well after the fourth pulse through third order in the interaction

$$\tilde{V}(t) = e^{iH(t - t_3)} V(t) e^{-iH(t - t_3)} \tag{12}$$

Projecting out the f-state amplitude gives

$$\begin{aligned}\langle f|\tilde{\Psi}(t \gg t_4)\rangle = \Big(&-i \int_{-\infty}^{\infty} d\tau \langle f|\tilde{V}(\tau)|g\rangle - \\ &\int_{-\infty}^{\infty} d\tau \int_{-\infty}^{\tau} d\tau' \langle f|\tilde{V}(\tau)\tilde{V}(\tau')|g\rangle + \\ i \int_{-\infty}^{\infty} d\tau \int_{-\infty}^{\tau} d\tau' &\int_{-\infty}^{\tau'} d\tau'' \langle f|\tilde{V}(\tau)\tilde{V}(\tau')\tilde{V}(\tau'')|g\rangle\Big) |n_g\rangle\end{aligned} \tag{13}$$

As detailed in the Appendix, this general expression can be made more explicit by accounting for the finite spectral bandwidth of the pulses. The resulting f-state amplitude is a linear superposition of 2 one-pulse and 10 three-pulse nuclear wave packets (but no two-pulse wave packets, because none of the

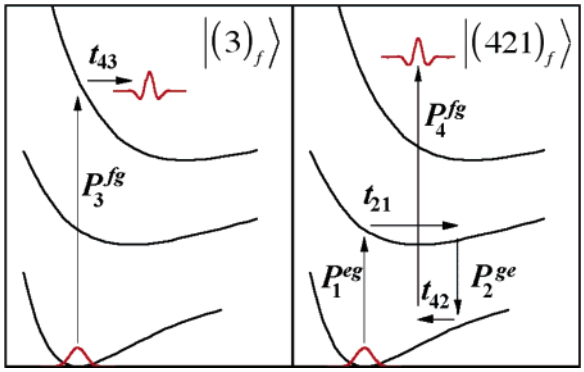

Figure 2. Excitations occurring in a two-color nonlinear WPI experiment. Vertical arrows denote electronic transitions; horizontal arrows denote time evolution. The first pulse-pair drives e ↔ g transitions, while the second drives f ← g. Left panel shows preparation of $|(3)_f\rangle$ through one-pulse excitation to the f state by the third pulse followed by propagation for t_{43}. Right panel depicts preparation of the three-pulse wave packet $|(421)_f\rangle$: first pulse transfers amplitude into the e state, where it propagates for t_{21}; a second pulse de-excites the wave packet to g, where it evolves for t_{42}; and a fourth pulse transfers the wave packet to the f state. The overlap of these wave packets makes the sought-after quadrilinear interference contribution to the f-state population (one of two quadrilinear overlaps).

pulses is resonant with f ↔ e). Returning to the Schrödinger picture, we have

$$\langle f|\Psi(t\gg t_4)\rangle = e^{-iH_f(t-t_4)}[|(3)_f\rangle + |(4)_f\rangle e^{-i\phi'} + |(421)_f\rangle e^{i\phi-i\phi'} + |(321)_f\rangle e^{i\phi} + |(411)_f\rangle e^{-i\phi'} + |(422)_f\rangle e^{-i\phi'} + |(311)_f\rangle + |(322)_f\rangle + |(333)_f\rangle + |(433)_f\rangle e^{-i\phi'} + |(443)_f\rangle + |(444)_f\rangle e^{-i\phi'}] \quad (14)$$

Equation 14 adopts an abbreviated notation to indicate the sequence of pulse action and free evolution giving rise to each wave packet. For example, the nuclear wave packet of first order in the third pulse alone is

$$|(3)_f\rangle = e^{-iH_f t_{43}} P_3^{fg} |n_g\rangle \quad (15)$$

while the wave packet trilinear in the first, second, and fourth pulses is

$$|(421)_f\rangle = P_4^{fg} e^{-iH_g t_{42}} P_2^{ge} e^{-iH_e t_{21}} P_1^{eg} e^{iH_g t_{31}} |n_g\rangle \quad (16)$$

Equations 15 and 16 use pulse propagators, with electronic matrix elements[52]

$$P_j^{ba} = \frac{i}{2}\int_{-\infty}^{\infty} d\tau A_j(\tau) e^{-i\Phi_j(\tau)} e^{iH_b\tau} \boldsymbol{\mu}_{ba}\cdot\mathbf{e}_j e^{-iH_a\tau} \quad (17)$$

to describe the shaping and transfer of nuclear amplitude by the jth pulse during the upward b ← a electronic transition. The downward b → a transition is governed by $P_j^{ab} = -P_j^{ba\dagger}$. Since the dependence of each term in eq 14 on the optical phase shifts (7) and (8) is indicated explicitly, the individual amplitudes are to be evaluated with both phase angles set to zero.[53] The sequences of pulse action and free propagation leading to $|(3)_f\rangle$ and $|(421)_f\rangle$ are illustrated in Figure 2. Expressions for the other terms in the f-state amplitude are given in the Appendix.

The f-state population is the measured quantity in a WPI experiment. As determined from eq 14, it can be expressed as a power series in the two optical phase factors

$$P_f(\phi,\phi') = |\langle f|\Psi(t)\rangle|^2 = \sum_{m=-1}^{1}\sum_{n=-1}^{1} p_{mn} e^{i(m\phi+n\phi')} \quad (18)$$

in which the coefficients are

$$p_{0,0} = \langle(3)_f|(3)_f\rangle + \langle(4)_f|(4)_f\rangle + [\langle(333)_f|(3)_f\rangle + \langle(444)_f|(4)_f\rangle + \langle(311)_f|(3)_f\rangle + \langle(411)_f|(4)_f\rangle + \langle(322)_f|(3)_f\rangle + \langle(422)_f|(4)_f\rangle + \langle(443)_f|(3)_f\rangle + \langle(433)_f|(4)_f\rangle + \text{c.c.}] \quad (19)$$

$$p_{1,0} = \langle(421)_f|(4)_f\rangle^* + \langle(321)_f|(3)_f\rangle^* \quad (20)$$

$$p_{0,1} = \langle(4)_f|(3)_f\rangle + \langle(422)_f|(3)_f\rangle + \langle(311)_f|(4)_f\rangle^* + \langle(433)_f|(3)_f\rangle + \langle(333)_f|(4)_f\rangle^* + \langle(443)_f|(4)_f\rangle^* + \langle(411)_f|(3)_f\rangle + \langle(444)_f|(3)_f\rangle + \langle(322)_f|(4)_f\rangle^* \quad (21)$$

$$p_{1,1} = \langle(321)_f|(4)_f\rangle^* \quad (22)$$

$$p_{-1,1} = \langle(421)_f|(3)_f\rangle \quad (23)$$

The remaining coefficients follow from $p_{-m,-n} = p_{m,n}^*$. Among these nine coefficients, $p_{-1,1}$ will be of specific interest for state reconstruction; it represents the overlap between a one-pulse wave packet prepared by the third pulse and a three-pulse wave packet resulting from sequential action of the first, second, and fourth pulses.

The coefficients p_{mn} of the Fourier series (18) could be determined according to the inversion formula[54]

$$p_{mn} = \frac{1}{4\pi^2}\int_0^{2\pi} d\phi \int_0^{2\pi} d\phi' P_f(\phi,\phi') e^{-i(m\phi+n\phi')} \quad (24)$$

Though formally exact, eq 24 is experimentally impractical, as it requires continuous sampling of the f-state population with respect to both optical phase shifts. It is more realistic to imagine that the f-state population can be sampled at evenly spaced discrete values of the phase shifts. ϕ and ϕ' can be taken as integer multiples of $\Delta = 2\pi/K$ (assumed to be the same for both phase angles)

$$\phi_j = j\Delta \quad \text{and} \quad \phi'_k = k\Delta \quad (25)$$

with $j,k = 0, 1, 2, ..., K-1$. We "approximate" each integral (24) as a sum over the evenly sampled phases

$$p_{mn} = \frac{\Delta^2}{4\pi^2}\sum_{j=0}^{K-1}\sum_{k=0}^{K-1} P_f(\phi_j,\phi'_k) e^{-i(m\phi_j+n\phi'_k)} \quad (26)$$

There are nine independent quantities on the right sides of eqs 19−23, so populations for at least nine distinct phase combinations (ϕ_j,ϕ'_k) should be sufficient. Trying $K = 3$ (i.e., $K^2 = 9$) in eq 26, we get

$$p_{mn} = \frac{1}{9}\sum_{j=0}^{2}\sum_{k=0}^{2} P_f(j\Delta,k\Delta) e^{-i(mj+nk)\Delta} \quad (27)$$

It can be seen that this prescription gives an exact, rather than approximate isolation of p_{mn}, due to the absence of higher multiples of the optical phase on the right hand side of eq 18.

The sought-after overlap (23) can be isolated by combining f-state population measurements

$$p_{-1,1} = \frac{1}{9}(P_f(0,0) + P_f(0,\Delta)e^{-i\Delta} + P_f(0,2\Delta)e^{i\Delta} + P_f(\Delta,0)e^{i\Delta} + P_f(\Delta,\Delta) + P_f(\Delta,2\Delta)e^{-i\Delta} + P_f(2\Delta,0)e^{-i\Delta} + P_f(2\Delta,\Delta)e^{i\Delta} + P_f(2\Delta,2\Delta)) \quad (28)$$

with $\Delta = 2\pi/3$. The ability to isolate the single overlap $\langle(421)_f|(3)_f\rangle$ by phase cycling in two-color nonlinear WPI is an improvement over the one-color case, where an additional overlap $\langle(431)_f|(2)_f\rangle$ bears the same $\exp(i\phi' - i\phi)$ phase signature and need not vanish in general.[39,43]

III. Target-State Reconstruction

The starting point for state reconstruction is the two-dimensional interferogram comprising the experimentally isolable overlaps $\langle(421)_f|(3)_f\rangle = p_{-1,1}$ of eq 28 for a range of t_{21} and t_{32} delays. These can be expressed as overlaps between an unknown one-pulse target state and a known three-pulse reference state

$$\langle(421)_f|(3)_f\rangle = \langle \mathrm{ref}_{421}(n_g)|\mathrm{tar}_3(n_g)\rangle \quad (29)$$

The target state

$$|\mathrm{tar}_3(n_g)\rangle = e^{i\phi_3(\omega'_L)+i\omega'_L t_{43}}|(3)_f\rangle \quad (30)$$
$$= e^{i\phi_3(\omega'_L)+i\omega'_L t_{43}} e^{-iH_f t_{43}} P_3^{fg}|n_g\rangle$$

is the nuclear wave packet prepared by the action of the third pulse on the initial nuclear state followed by propagation under the unknown f-state Hamiltonian for a time fixed delay t_{43}. The spectral phase $\phi_3(\omega'_L)$ is introduced in eq 30 to remove dependence on the uncontrolled absolute phase of the third pulse, i.e., $\Phi_3(0)$. The variable reference states

$$|\mathrm{ref}_{421}(n_g)\rangle = e^{i\phi_4(\omega'_L)}|(421)_f\rangle \quad (31)$$
$$= e^{i\phi_4(\omega'_L)} P_4^{fg}\, e^{-iH_g t_{42}} P_2^{ge}\, e^{-iH_e t_{21}} P_1^{eg}\, e^{iH_g t_{31}}|n_g\rangle$$

incorporate the same phase factor appearing in eq 30, and are otherwise defined by their successive intervals, t_{21} and $t_{32} + t_{43}$, of e-state and g-state evolution (see Figure 2). Recall that the isolable overlap is defined with ϕ' (and ϕ) equal to zero, so that $\phi_4(\omega'_L) = \phi_3(\omega'_L) + \omega'_L t_{43}$ from eq 8.

For purposes of target-state reconstruction, the two-dimensional interferogram can be reorganized to form M singly indexed elements $z_m = \langle \mathrm{ref}_{421}(n_g)|\mathrm{tar}_3(n_g)\rangle$ of a signal vector, where $m \equiv (t_{21},t_{32})$. We represent the target and reference states in a discrete position basis $\{|x_n\rangle, n = 1, 2, ..., N\}$ of uniform spacing $\Delta x = x_{n+1} - x_n$. With the completeness relation for position eigenstates, we may express the signal elements as

$$z_m = \sum_n \langle \mathrm{ref}_{421}(n_g)|x_n\rangle\langle x_n|\mathrm{tar}_3(n_g)\rangle \Delta x \quad (32)$$

from where

$$\mathbf{z} = \mathbf{R}\mathbf{t} \quad (33)$$

where the row elements of the $M \times N$ reference matrix $R_{mn} = \langle \mathrm{ref}_{421}|x_n\rangle\Delta x$ represent the conjugate wave functions of the reference states and the N-dimensional target vector $t_n = \langle x_n|\mathrm{tar}_3\rangle$ represents the target wave function.

To reconstruct the target from the measured interference signal, we invert eq 33 using our knowledge of the reference matrix. As the reference matrix may be singular or nearly so, this inversion is performed using singular value decomposition.[56] The reference matrix is partitioned as

$$\mathbf{R} = \mathbf{U}\mathbf{W}\mathbf{V}^\dagger \quad (34)$$

where the $N \times N$ matrix $\mathbf{V}$ is unitary, the $M \times N$ matrix $\mathbf{U}$ is row unitary, and the real $N \times N$ matrix $\mathbf{W}$ is diagonal with singular values$W_{jj} \geq 0$. If any singular value is zero, the inverse of $\mathbf{R}$ is not defined, but a pseudoinverse of $\mathbf{R}$ can be constructed as

$$\mathbf{R}_T^{-1} = \mathbf{V}\mathbf{W}_T^{-1}\mathbf{U}^\dagger \quad (35)$$

$\mathbf{W}_T^{-1}$ is a modified inverse with elements

$$(\mathbf{W}_T^{-1})_{jj} = \begin{cases} 1/W_{jj} & \text{if } W_{jj}/W_{\max} > T \\ 0 & \text{otherwise} \end{cases} \quad (36)$$

where $W_{\max}$ is the largest singular value and T is a chosen tolerance.[57] The solution to eq 33 obtained by applying the pseudoinverse of the reference matrix to the signal vector

$$\mathbf{r} = \mathbf{R}_T^{-1}\mathbf{z} \quad (37)$$

minimizes the norm $|\mathbf{r}|$ and the residual $|\mathbf{z} - \mathbf{R}\mathbf{r}|$.[56] To quantify the accuracy of the reconstructed wave packet, we define the fidelity

$$f = \frac{|\mathbf{r}^\dagger \cdot \mathbf{t}|}{|\mathbf{r}||\mathbf{t}|} \quad (38)$$

which lies between 0 and 1.

Our signal isolation and state reconstruction procedure can be extended to a mixed-state system described by an initial density matrix $\rho_g = \sum w_{n_g}|n_g\rangle\langle n_g|$.[45] Here the f-state population comprises the simultaneous contributions of multiple $P_f^{n_g}$ akin to eq 18, each originating from a different initial rovibrational level n_g and weighted by its population w_{n_g}

$$P_f(\phi,\phi') = \sum w_{n_g} P_f^{n_g}(\phi,\phi') \quad (39)$$

All of the terms in eq 39 exhibit the same phase-shift dependences as in the pure-state case, so the phase-cycled signal combination (28) now yields an initial-population-weighted sum of quadrilinear interferences of the form (29). The elements of a signal "vector" analogous to eq 32 can now be written as

$$z_m = \sum_{n_g}\sum_n w_{n_g}\langle \mathrm{ref}_{421}(n_g)|x_n\rangle\langle x_n|\mathrm{tar}_3(n_g)\rangle \Delta x \quad (40)$$

Reconstruction of the mixed-state targets proceeds as before, but with the ensemble of target states represented by a KN-dimensional vector $t_l = \langle x_k|\mathrm{tar}_3(n_g)\rangle$, and the reference states stored in a $M \times KN$ matrix $R_{ml} = w_{n_g}\langle \mathrm{ref}_{421}(n_g)|x_k\rangle\Delta x$, where K is the number of populated initial states and $l \equiv (k,n_g)$. Inverting eq 40 yields a KN-dimensional reconstructed vector of the same structure as the target, whose quality can be characterized by an average fidelity $f = \sum w_{n_g} f_{n_g}$.

IV. Diatomic Molecule

A diatomic molecule in the gas phase with accurately known internuclear potentials would be a natural candidate for initial experiments testing state reconstruction by nonlinear WPI. In

this section, we obtain expressions for the rovibrational target and reference states of a diatomic molecule, specializing to the case of zero electronic angular momentum, i.e., $^1\Sigma$ electronic levels. The nuclear Hamiltonian of the a electronic level (a = g, e, f) may be written as[58]

$$H_a = -\frac{1}{2\mu R}\frac{\partial^2}{\partial R^2}R + \frac{\mathbf{J}^2}{2\mu R^2} + U_a(R) \tag{41}$$

where $U_a(R)$ is the internuclear potential, $\mathbf{J}$ is the total angular momentum operator, and μ is the reduced mass. The angular momentum satisfies $\mathbf{J}^2|J,M\rangle = J(J+1)|J,M\rangle$ and $J_z|J,M\rangle = M|J,M\rangle$, with J a nonnegative integer and M taking integral values from $-J$ to J. As H_a and $\mathbf{J}^2$ commute, the eigenstates of (41) are tensor products of rotational and vibrational components

$$|n_a(v,J,M)\rangle = |v(J)\rangle|J,M\rangle \tag{42}$$

where $|v(J)\rangle$ is an eigenstate of the vibrational Hamiltonian

$$H_a(J) = \langle J,M|H_a|J,M\rangle = -\frac{1}{2\mu R}\frac{\partial^2}{\partial R^2}R + \frac{J(J+1)}{2\mu R^2} + U_a(R) \tag{43}$$

To evaluate the target and reference states (30) and (31), we calculate rotational matrix elements of the pulse propagators (17)

$$\langle J',M'|P_j^{ba}|J,M\rangle = \frac{i}{2}\int_{-\infty}^{\infty} d\tau A_j(\tau)e^{-i\Phi_j(\tau)}e^{iH_b(J')\tau}\langle J',M'|\boldsymbol{\mu}_{ba}\cdot\mathbf{e}_j|J,M\rangle e^{-iH_a(J)\tau} \tag{44}$$

With the polarization vector along the space-fixed z axis, we have

$$\langle J',M'|\boldsymbol{\mu}_{ba}\cdot\mathbf{e}_j|J,M\rangle = \mu_{ba}(R)\langle J',M'|\cos\theta|J,M\rangle \tag{45}$$
$$= \mu_{ba}(R)\delta_{M',M}[c(J+1,M)\delta_{J',J+1} + c(J,M)\delta_{J',J-1}]$$

in which $\mu_{ba}(R)$ specifies the internuclear coordinate dependence of the transition dipole moment and $c(J,M) = \sqrt{(J^2-M^2)/(4J^2-1)}$. Insertion in eq 44 gives

$$\langle J',M'|P_j^{ba}|J,M\rangle = c(J+1,M)\mathscr{R}_j^{ba}(J)\delta_{J',J+1}\delta_{M',M} + c(J,M)\mathscr{P}_j^{ba}(J)\delta_{J',J-1}\delta_{M',M} \tag{46}$$

with J-dependent vibrational operators

$$\mathscr{R}_j^{ba}(J) = \frac{i}{2}\int_{-\infty}^{\infty} d\tau A_j(\tau)e^{-i\Phi_j(\tau)}e^{iH_b(J+1)\tau}\mu_{ba}(R)e^{-iH_a(J)\tau} \tag{47}$$

and

$$\mathscr{P}_j^{ba}(J) = \frac{i}{2}\int_{-\infty}^{\infty} d\tau A_j(\tau)e^{-i\Phi_j(\tau)}e^{iH_b(J-1)\tau}\mu_{ba}(R)e^{-iH_a(J)\tau} \tag{48}$$

Using eq 46, we can express the target state as

$$|\mathrm{tar}_3(v,J,M)\rangle = c(J+1,M)|\chi_+(v,J)\rangle|J+1,M\rangle + c(J,M)|\chi_-(v,J)\rangle|J-1,M\rangle \tag{49}$$

where

$$|\chi_+(v,J)\rangle = e^{i(\phi_3(\omega'_L)+\omega'_L t_{43})}e^{-iH_f(J+1)t_{43}}\mathscr{R}_3^{fg}(J)|v(J)\rangle \tag{50}$$

and

$$|\chi_-(v,J)\rangle = e^{i(\phi_3(\omega'_L)+\omega'_L t_{43})}e^{-iH_f(J-1)t_{43}}\mathscr{P}_3^{fg}(J)|v(J)\rangle \tag{51}$$

The centrifugal potential differs in the (f,J+1) and (f,J−1) states, and because of the small resulting difference in transition energy from the (g,J) state, the starting wave packets $\mathscr{R}_3^{fg}(J)|v(J)\rangle$ and $\mathscr{P}_3^{fg}(J)|v(J)\rangle$ may not exactly coincide. Greater differences between the target components $|\chi_+(v,J)\rangle$ and $|\chi_-(v,J)\rangle$ can arise from their propagation for t_{43} under these differing potentials.

Reference states found from eqs 31 and 46 have ($J \pm 1$) and ($J \pm 3$) components, but the latter can be omitted due to their orthogonality with the target state:

$$|\mathrm{ref}_{421}(v,J,M)\rangle = \{c(J+1,M)c(J,M)^2|\delta_2(v,J)\rangle + c(J+1,M)^3|\delta_3(v,J)\rangle + c(J+1,M)c(J+2,M)^2|\delta_4(v,J)\rangle\}|J+1,M\rangle + \{c(J,M)c(J-1,M)^2|\delta_5(v,J)\rangle + c(J,M)^3|\delta_6(v,J)\rangle + c(J,M)c(J+1,M)^2|\delta_7(v,J)\rangle\}|J-1,M\rangle \tag{52}$$

The vibrational wave packets accompanying different sequences of rotational transitions are given by

$$|\delta_2(v,J)\rangle = e^{i\phi_4(\omega'_L)}\mathscr{R}_4^{fg}(J)e^{-iH_g(J)t_{42}}\mathscr{R}_2^{ge}(J-1)e^{-iH_e(J-1)t_{21}}\mathscr{P}_1^{eg}(J)e^{iH_g(J)t_{31}}|v(J)\rangle \tag{53}$$

$$|\delta_3(v,J)\rangle = e^{i\phi_4(\omega'_L)}\mathscr{R}_4^{fg}(J)e^{-iH_g(J)t_{42}}\mathscr{P}_2^{ge}(J+1)e^{-iH_e(J+1)t_{21}}\mathscr{R}_1^{eg}(J)e^{iH_g(J)t_{31}}|v(J)\rangle \tag{54}$$

$$|\delta_4(v,J)\rangle = e^{i\phi_4(\omega'_L)}\mathscr{P}_4^{fg}(J+2)e^{-iH_g(J+2)t_{42}}\mathscr{R}_2^{ge}(J+1)e^{-iH_e(J+1)t_{21}}\mathscr{R}_1^{eg}(J)e^{iH_g(J)t_{31}}|v(J)\rangle \tag{55}$$

$$|\delta_5(v,J)\rangle = e^{i\phi_4(\omega'_L)}\mathscr{R}_4^{fg}(J-2)e^{-iH_g(J-2)t_{42}}\mathscr{P}_2^{ge}(J-1)e^{-iH_e(J-1)t_{21}}\mathscr{P}_1^{eg}(J)e^{iH_g(J)t_{31}}|v(J)\rangle \tag{56}$$

$$|\delta_6(v,J)\rangle = e^{i\phi_4(\omega'_L)}\mathscr{P}_4^{fg}(J)e^{-iH_g(J)t_{42}}\mathscr{R}_2^{ge}(J-1)e^{-iH_e(J-1)t_{21}}\mathscr{P}_1^{eg}(J)e^{iH_g(J)t_{31}}|v(J)\rangle \tag{57}$$

$$|\delta_7(v,J)\rangle = e^{i\phi_4(\omega'_L)}\mathscr{P}_4^{fg}(J)e^{-iH_g(J)t_{42}}\mathscr{P}_2^{ge}(J+1)e^{-iH_e(J+1)t_{21}}\mathscr{R}_1^{eg}(J)e^{iH_g(J)t_{31}}|v(J)\rangle \tag{58}$$

Note that for the downward transitions, $\mathscr{R}_j^{eg}(J) = -\mathscr{P}_j^{eg}(J+1)^\dagger$ and $\mathscr{P}_j^{eg}(J) = -\mathscr{R}_j^{eg}(J-1)^\dagger$, as is consistent with eq 17 and the comments following. Expressions similar to (53−58) can easily be given for the vibrational amplitudes $|\delta_1\rangle$ and $|\delta_8\rangle$ accompanying the unused $J+3$ and $J-3$ components, respectively.

The overlap of target and reference states is given by

$$\langle\mathrm{ref}_{421}(v,J,M)|\mathrm{tar}_3(v,J,M)\rangle = q_M(J+1,J)\langle\delta_2(v,J)|\chi_+(v,J)\rangle + q_M(J+1,J+1)\langle\delta_3(v,J)|\chi_+(v,J)\rangle + q_M(J+2,J+1)\langle\delta_4(v,J)|\chi_+(v,J)\rangle + q_M(J,J-1)\langle\delta_5(v,J)|\chi_-(v,J)\rangle + q_M(J,J)\langle\delta_6(v,J)|\chi_-(v,J)\rangle + q_M(J+1,J)\langle\delta_7(v,J)|\chi_-(v,J)\rangle \tag{59}$$

with M-dependent weighting factors

$$q_M(J_1,J_2) = c(J_1,M)^2c(J_2,M)^2 \tag{60}$$

The quadrilinear overlap (59) is the desired nonlinear WPI signal from a pure (v,J,M) initial state. Even at the low temperatures common to molecular beams, multiple rotational levels are ordinarily populated, and we must sum over contributions from thermally occupied (J,M) states to obtain the measured signal. Initial states with the same v and J make an aggregate contribution

$$\sum_{M=-J}^{J} \langle \mathrm{ref}_{421}(v,J,M)|\mathrm{tar}_3(v,J,M)\rangle = \langle \delta_+(v,J)|\chi_+(v,J)\rangle + \langle \delta_-(v,J)|\chi_-(v,J)\rangle \quad (61)$$

The effective vibrational reference packets appearing in eq 61 are defined by

$$|\delta_+(v,J)\rangle = b_J(J+1,J)|\delta_2\rangle + b_J(J+1,J+1)|\delta_3\rangle + b_J(J+2,J+1)|\delta_4\rangle \quad (62)$$

and

$$|\delta_-(v,J)\rangle = b_J(J,J-1)|\delta_5\rangle + b_J(J,J)|\delta_6\rangle + b_J(J+1,J)|\delta_7\rangle \quad (63)$$

where[59]

$$b_J(J_1,J_2) = \sum_{M=-J}^{J} q_M(J_1,J_2) = \frac{1}{(4J_1^2-1)(4J_2^2-1)} \times \left[J_1^2J_2^2(2J+1) - (J_1^2+J_2^2)\frac{J}{3}(J+1)(2J+1) + \frac{J}{15}(J+1)(2J+1)(3J^2+3J-1)\right] \quad (64)$$

For the general case of a homonuclear diatomic molecule at thermal equilibrium, we can obtain the interference signal as a Boltzmann-weighted sum over eq 61

$$z_m = \sum_v \sum_J w_{vJ}[\langle \delta_+(v,J)|\chi_+(v,J)\rangle + \langle \delta_-(v,J)|\chi_-(v,J)\rangle] \quad (65)$$

Here $w_{vJ} = g_J(I)e^{-\beta E_g(v,J)}/Z$, $\beta = 1/kT$, and $g_J(I)$ is a degeneracy factor dependent on the nuclear spin I.[60]

V. Li_2

To test our reconstruction method, we calculate the nonlinear WPI signal for the lithium dimer and demonstrate the direct determination of a rovibrational target state from this signal. Accurate ab initio potentials for the $X(^1\Sigma_g^+)$, $A(^1\Sigma_u^+)$, and $E(^1\Sigma_g^+)$ electronic levels[46] are shown in Figure 3. At large internuclear distances, the E-state potential exhibits a shelf region where the spacing between vibrational and rotational energy levels can become similar in size. Even at the slightly smaller range of distances traversed by our target wave packet, vibration−rotation coupling significantly influences the dynamics. Since rotational and vibrational motion cannot be separated, the dynamics of the target wave packet that we seek to reconstruct is genuinely multidimensional, rather than being describable as a product of independent rotations and vibrations.

In our calculations, the initial states are the ($v_A = 8$, $J_A = 18$, M_A) eigenstates of the A electronic level, whose vibrational component is shown in Figure 3. Leone and co-workers have used such "launch states" as precursors for time-dependent wave packet studies.[47−51] In those experiments, a continuous-wave laser excites a selected A ← X rovibronic transition to populate a launch state, and a subsequent (shaped) ultrashort laser pulse excites a rovibrational wave packet on the E-state potential curve.

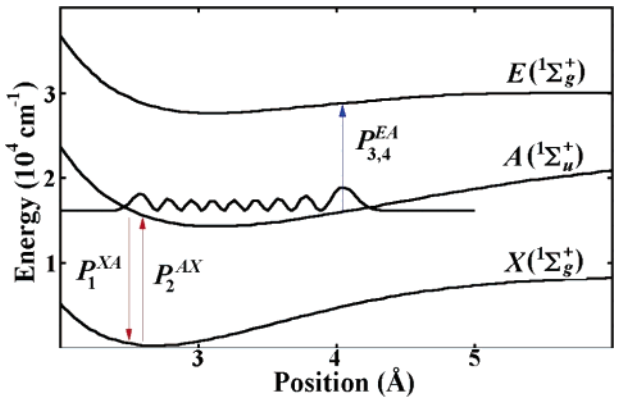

Figure 3. X, A, and E potential energy curves of Li_2, interpolated from the data of ref 46. In our calculations, the initial states are the ($v_A = 8$, $J_A = 18$, M_A) nuclear eigenstates of the A electronic level. The radial component of the launch states is plotted as $R\langle R|v_A(J_A)\rangle$ and vertically displaced by its eigenenergy. Vertical arrows at the inner and outer turning points indicate the electronic transitions driven by the first (red) and second (blue) pulse pairs, respectively.

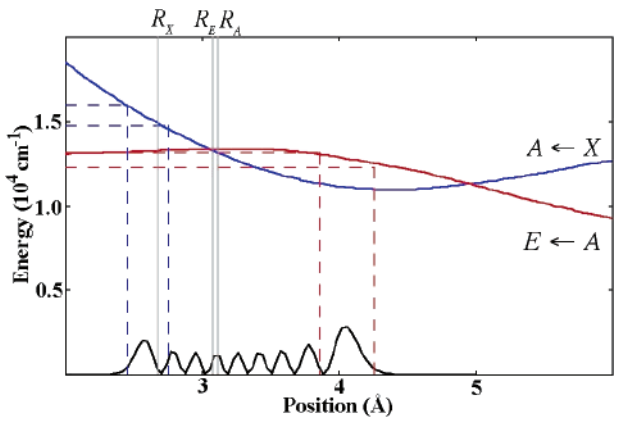

Figure 4. Spatial ranges of electronic resonance for pulses 1, 2, and 3. The A minus X (solid blue line) and E minus A (solid red line) difference potentials are plotted, along with $R\langle R|v_A(J_A)\rangle$ (solid black line). Members of the first pulse-pair resonate with the A ← X difference potential from 2.4 to 2.7 Å, near the inner turning point of the launch state as denoted by the dashed (blue) lines. The third pulse, which prepares the target wave packet, is resonant with E ← A from 3.8 to 4.2 Å, near the launch state's outer turning point as denoted by the dashed (red) lines. The fourth pulse is shorter than the third and has a correspondingly broader range of resonance due to its increased spectral bandwidth (see text). Solid vertical lines indicate the equilibrium positions R_X, R_E, and R_A.

We choose the center frequency of the first (second) pulse pair to selectively excite electronic transitions at the inner (outer) turning point of the launch state. The jth field has amplitude $A_j(t) = A_j \exp(-t^2/2\sigma_j^2)$ and phase $\Phi_j(t) = \Phi_j + \Omega_j t$. The first pulse pair has carrier frequency $\Omega_{1,2} = 2\pi c(15384\ \mathrm{cm}^{-1})$, resonant with A ↔ X at 2.56 Å. With $\sigma_{1,2} = 10.00$ fs, the full width at half-maximum (fwhm) of the temporal envelope is 23.55 fs (spectral bandwidth $2\pi c$ (1250 cm^{-1}) fwhm in the amplitude). The second pulse pair has $\Omega_{3,4} = 2\pi c$ (12738 cm^{-1}), which is resonant with E ← A at 4.09 Å. The third pulse is of duration $\sigma_3 = 15.62$ fs (36.78 fs temporal amplitude fwhm, $2\pi c$ (800.3 cm^{-1}) spectral amplitude fwhm). We use a shorter fourth pulse, with $\sigma_4 = 6.01$ fs (14.15 fs temporal amplitude fwhm, $2\pi c$ (2080 cm^{-1}) spectral amplitude fwhm). Figure 4 uses the

reflection principle to identify the spatial range of resonance for pulses 1, 2, and 3.

In section II, the initial electronic level g was assumed to be lower in energy than the intermediate and final levels, e and f. In the case of Li_2, the initial level A is of higher energy than the "intermediate" X level. This difference in the ordering of the electronic levels changes the phase factor accompanying the three-pulse wave packet $|(421)_E\rangle$ in eq 14 from $\exp(i\phi - i\phi')$ to $\exp(-i\phi - i\phi')$. The change occurs because the first pulse now drives a downward transition and the second drives an upward transition, rather than vice versa. The factor accompanying $|(321)_E\rangle$ also changes, from $\exp(i\phi)$ to $\exp(-i\phi)$, while the $\exp(-i\phi')$ accompanying $|(4)_E\rangle$ is unchanged. The desired quadrilinear overlap

$$\langle(421)_E|(3)_E\rangle = p_{-1,-1} \tag{66}$$

therefore remains isolable by phase cycling, according to the prescription (26), as it is the only contribution to the E-state population with $\exp(-i\phi - i\phi')$ as its phase signature. The isolated overlap (66) can be rewritten in terms of target and reference states whose definitions are independent of the uncontrolled absolute optical phase, as in eq 29. From eq 30 the target wave packet is given by

$$|\mathrm{tar}_3(\upsilon_A,J_A,M_A)\rangle = e^{i\phi_3(\omega'_L)+i\omega'_L t_{43}} e^{-iH_E t_{43}} P_3^{EA} |\upsilon_A(J_A)\rangle|J_A,M_A\rangle \tag{67}$$

while from eq 31 the reference states are

$$|\mathrm{ref}_{421}(\upsilon_A,J_A,M_A)\rangle = e^{i\phi_4(\omega'_L)} P_4^{EA} e^{-iH_A t_{42}} P_2^{AX} e^{-iH_X t_{21}} P_1^{XA} e^{iH_A t_{31}} |\upsilon_A(J_A)\rangle|J_A,M_A\rangle \tag{68}$$

The wave packets were propagated using the J-dependent vibrational Hamiltonians (43), with X, A, and E potential energy curves obtained by numerically interpolating the ab initio data of Schmidt-Mink et al.[46] We used a spatial grid of 256 equally spaced points from 0.1 to 9.0 Å to calculate the wave packets (50), (51), (62), and (63) contributing on the right hand side of eq 61. Propagation was carried out using a split-operator approximation to the time-evolution operator with a time step of 0.01 fs.[55]

The pulse propagators (47) and (48) were also calculated in the discrete position basis. Time integration was approximated as a sum over the range of nonnegligible field amplitude with a $\Delta\tau = 0.01$ fs time increment. The time-evolution operators in the integrand were calculated using the split-operator approximation, with the free-particle portion expanded through order $\Delta\tau^{12}$ and the kinetic energy operator approximated as a second-order finite difference. The transition dipole moment functions were obtained by interpolating the data of ref 46 within the range 1.72−9 Å. The grid used for wave packet propagation extended beyond these limits, but owing to the finite bandwidth of the pulses, the pulse propagators transfer amplitude only within this more limited spatial range.

We chose $t_{43} = 18.84$ ps for the target-defining delay, approximately 100 vibrational periods in the E state. After this lengthy propagation, the magnitude of the overlap between the $J_A \pm 1$ target vibrational wave packets decays to 3.4% (from an initial value differing very slightly from unity due to the small difference in pulse propagators). As shown in Figure 5, both components of the target occupy the same spatial region, but their phases have opposite slopes, indicating that the $J_A + 1$ wave packet is traveling to the right and the $J_A - 1$ wave packet is traveling to the left. Wigner distribution functions for the target-state components are shown superimposed on phase-space energy contours for E-state motion in Figure 6. Both Wigner plots are far from Gaussian and have both positive and negative regions, in keeping with the highly nonclassical nature of the target components.

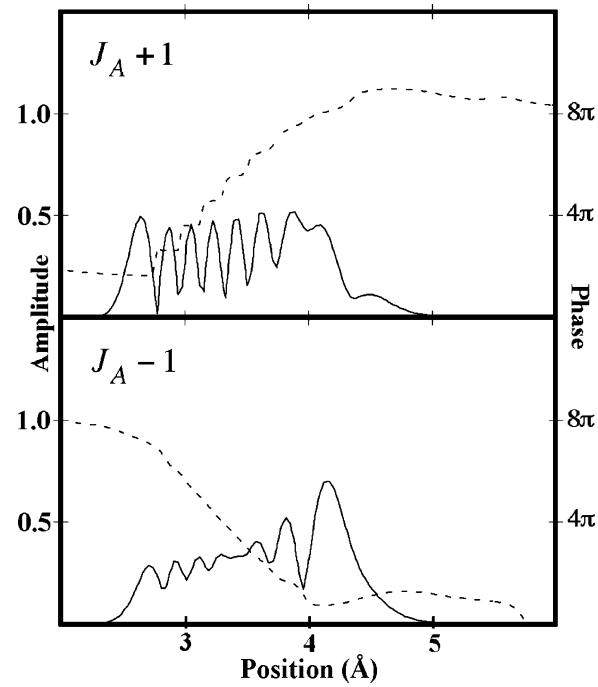

Figure 5. Amplitude (solid line) and phase (dashed line) of the target-state vibrational components after 18.84 ps of E-state propagation. The slope of the quantum mechanical phase function indicates that the $J_A + 1$ ($J_A - 1$) wave packet is traveling to the right (left).

Reference states were calculated for t_{21} and t_{32} between 0 and 600 fs at intervals of 4 fs (for a total of $150 \times 150 = 22500$ signal points). The calculated reference-state components at given t_{21} and t_{32}, $|\delta_+(\upsilon_A,J_A)\rangle$ and $|\delta_-(\upsilon_A,J_A)\rangle$, were stored together in a row of the reference matrix. To compensate for overweighting of the $J_A + 1$ component of the reference state due to rotational selection rules, $|\delta_-(\upsilon_A,J_A)\rangle$ was multiplied by the scaling factor, a_{J_A}, where

$$a_J = \left(\frac{b_J(J+1,J) + b_J(J+1,J+1) + b_J(J+2,J+1)}{b_J(J,J-1) + b_J(J,J) + b_J(J+1,J)}\right)^{1/2} \tag{69}$$

$b_J(J_1,J_2)$ is defined in eq 64. The $|\chi_-(\upsilon_A,J_A)\rangle$ component of the calculated target state was multiplied by a canceling factor, a_J^{-1} (the signal must remain unchanged), and the $J_A - 1$ component of the reconstructed target state was corrected by removing the same unwanted factor. This procedure is an approximate means of balancing the reference and target states so that in both sets of states the ratio of norms of the $J_A + 1$ and $J_A - 1$ components is about the same. Introducing a_J boosts reconstruction accuracy, particularly for small values of J. In our calculations, $J_A = 18$, and introducing the balancing factor, $a_{18} = 1.0274$, has a small favorable effect on the fidelity of reconstruction. It is important to emphasize that the value of a_J was chosen on the basis of rotational selection rules alone; no use was made of dynamical information specific to the preparation or propagation of the target wave packet on the E-state surface of Li_2.

The nonlinear WPI signal is generated by applying the calculated reference matrix to the calculated target vector. Figure

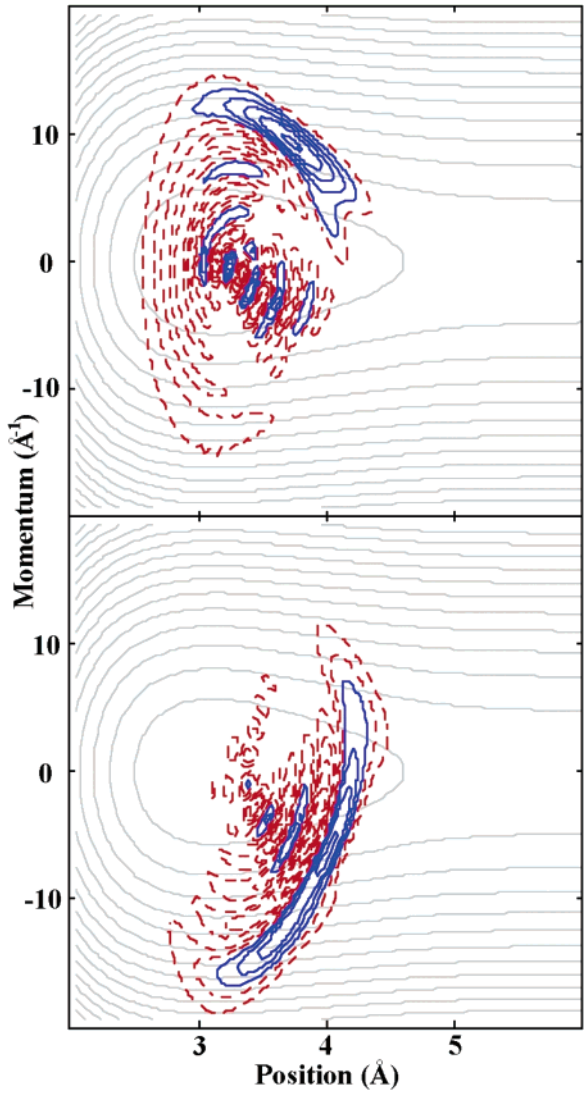

Figure 6. Wigner representations of the target-state vibrational components overlaid on isoenergy contours of the E electronic surface. The upper panel represents the $J_A + 1$ component of the target state, and the lower panel represents the $J_A - 1$ component. Energy contours are separated by 1000 cm^{-1}. Note that the average position of the two wave packets is similar but that they have opposite directions of motion. The differences between the two vibrational components result from vibration−rotation coupling and underline the genuine multidimensionality of the dynamics. The delocalized and non-Gaussian form of the Wigner distribution functions, with both positive (solid blue lines) and negative (dashed red lines) regions, illustrates the nonclassical nature of the vibrational states.

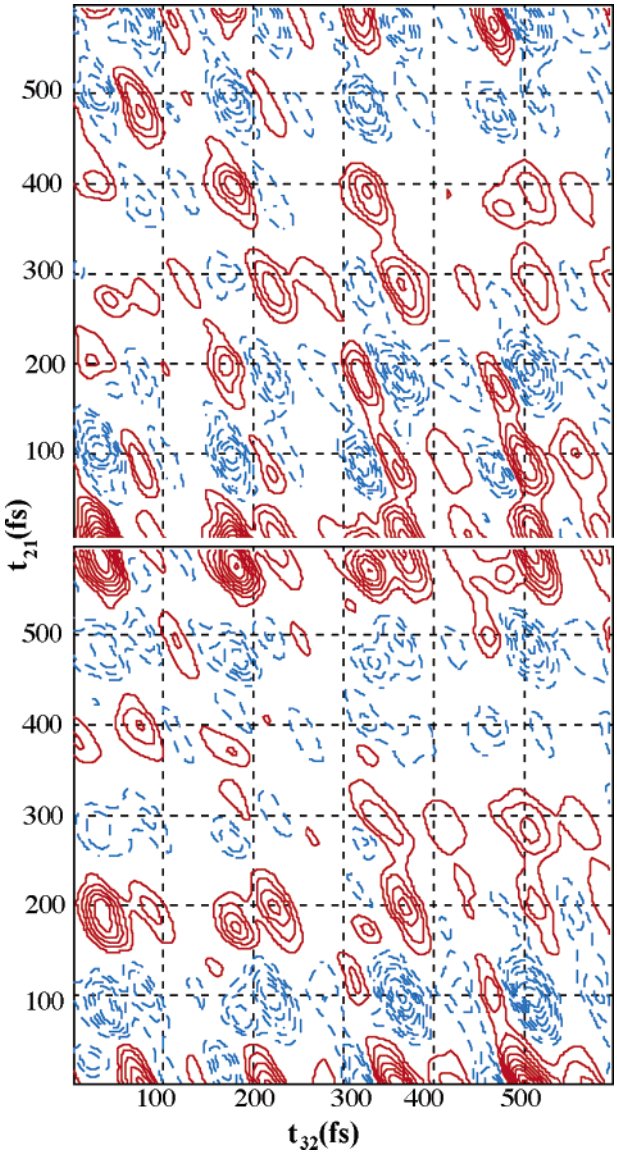

Figure 7. Real (upper panel) and imaginary (lower panel) components of the calculated interferogram for the lithium dimer as a function of the interpulse pulse delays t_{21} and t_{32} with fixed $t_{43} = 18.84$ ps. Both positive (solid red lines) and negative (dashed blue lines) contours are separated by $^1/_{10}$th of the maximum signal. The periodicity along each time axis reflects the periodic changes in the overlap of the variable reference state with the fixed target state shown in Figures 5 and 6.

7 plots the real and imaginary components of the resulting interferogram as a function of t_{21} and t_{32}. Both constructive and destructive wave packet interference effects are manifested in the presence of positive and negative regions in the interferogram. The interferogram is quasi-periodic along both t_{21} and t_{32} axes. At fixed t_{32}, the signal peaks roughly every 95 fs along t_{21}, which agrees with the vibrational period in the X state. This feature arises from the wave packets in the X level moving in and out of the spatial window defined by the bandwidth of the second pulse, as illustrated in Figure 4. The interferogram has a periodicity of 140 fs along t_{32}, corresponding with the period of motion in state A. A double peak consisting of two subpeaks separated by 44 fs appears with this period. The two subpeaks signal separate maxima in the magnitudes of $\langle\delta_+|\chi_+\rangle$ and $\langle\delta_-|\chi_-\rangle$, whose sum constitutes the interference signal. The spacing between the subpeaks corresponds to the time needed for a reference wave packet on the A surface to travel from the phase-space point of the $J_A + 1$ target-state component to that of the $J_A - 1$ component (see Figure 6). Thus, the temporal separation of these subpeaks directly reflects the influence of rotation−vibration coupling on the dynamics of the target state.

Reconstruction of the target state is carried out according to the procedure of section III. We carried out this procedure with a range of tolerance values to determine the optimal tolerance for reconstruction and found that unit fidelity is always achievable from a noise-free interferogram provided a sufficiently small tolerance ($\sim 10^{-10}$) is employed. To provide a more realistic test of the reconstruction technique, we applied 5% uncorrelated Gaussian noise to the interferogram. The resulting reconstructed state is plotted along with the target state in Figure 8.

The reconstructed state agrees very well with the target, reproducing it with fidelity 0.9980 (using a tolerance of 0.0417) despite the presence of 5% noise in the signal. Although the

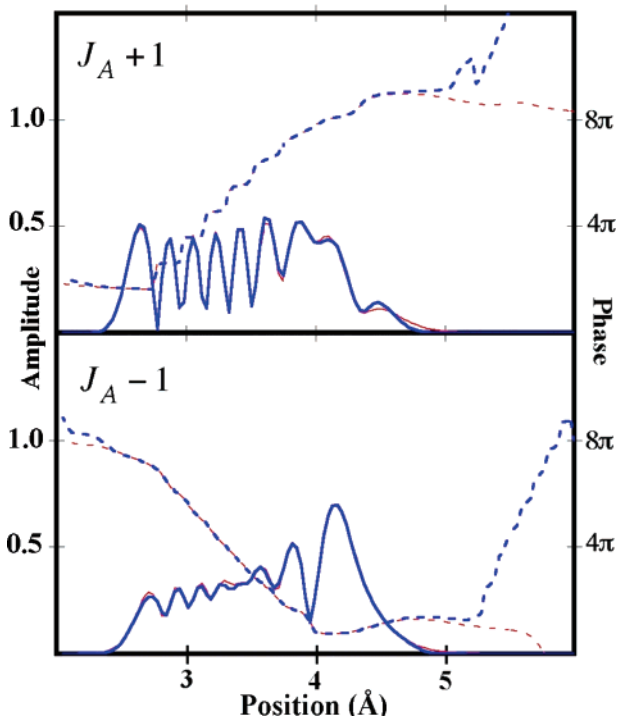

Figure 8. The amplitude (solid lines) and phase (dashed lines) of the $J_A + 1$ and $J_A - 1$ components of the target (red fine lines) and reconstructed (blue bold lines) wave packets. The left vertical axis measures amplitude, and the right vertical axis measures phase. The reconstructed state was obtained using the calculated interferogram of Figure 7 with 5% Gaussian noise added. The fidelity is 0.9983 with a tolerance of 0.0417.

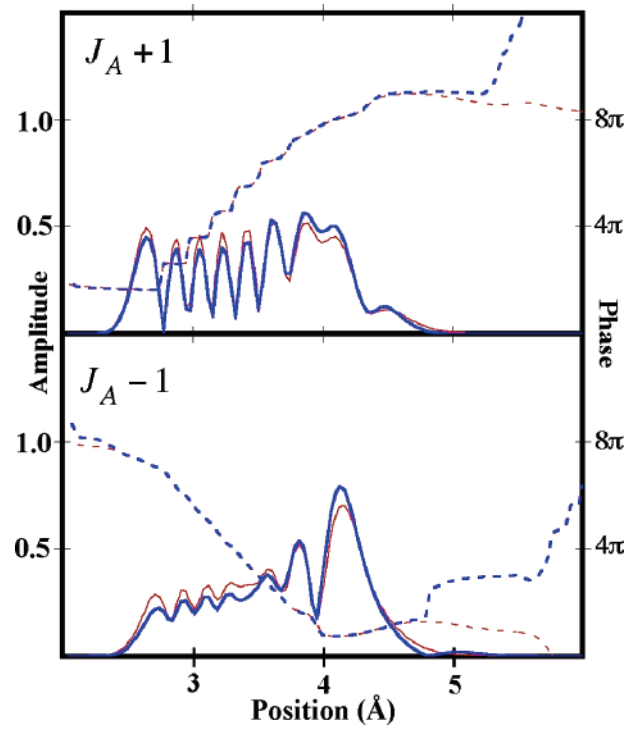

Figure 9. Same as Figure 8 except that approximate reference states calculated by assuming a constant difference potential between the A and E electronic levels are used in the reconstruction procedure. The resulting fidelity is 0.9907 with a tolerance of 0.0511.

phase structure of the reconstructed components is nearly perfect over the full spatial range of the wave packets, small errors in the amplitude are discernible, mostly at internuclear distances greater than about 4.0 Å. These amplitude deviations are attributable to the paucity of reference-state amplitude at large internuclear distance, due to the fact that the A-state potential has a more strongly attractive outer wall than the E state, which limits the outer range of motion of the reference wave packets. It is a consequence of the added signal noise that the optimal tolerance is larger than that in the noiseless case. This behavior is expected, since retaining small singular values in the presence of signal noise leads to a distortion of the reconstructed state in a futile attempt to reproduce noise having nothing to do with the actual target state.

A feature distinguishing nonlinear WPI from linear WPI is its capacity in principle to reconstruct a target wave packet even in the absence of complete information about the f-state nuclear Hamiltonian. Prior to the fourth pulse, the reference wave packet propagates only on the lower-lying g and e surfaces; although the fourth-pulse propagator, P_4^{fg}, depends formally upon H_f, this dependence can be suppressed by the brevity of the fourth pulse, which carries out the last step taken in preparing each reference state. With a sufficiently brief pulse 4, a crude approximation to the f-state potential can be sufficient for the calculation of P_4^{fg}.[45] For the lithium dimer, we investigate wave packet reconstruction using a propagator for pulse 4 calculated by assuming a constant E−A difference potential equal to $2\pi c$ (13345 cm^{-1}), the energy difference between the minima of the actual potentials. A pseudoinverse of the reference matrix calculated under this approximation is applied to the rigorously calculated signal in Figure 7 with 5% Gaussian noise added. The resulting reconstructed state, shown in Figure 9, has fidelity 0.9907 for a 0.0511 tolerance. Reconstruction of the spatial dependence of the target packet's phase remains very accurate, while the reconstructed amplitude shows some additional inaccuracy compared to the results obtained using the pseudo-inverse of the rigorous reference matrix (compare Figure 9 to Figure 8). The reconstructed state overestimates the target-state amplitude where the reference-state amplitude is underestimated by the approximate P_4^{fg} and vice versa.

The fact that the ∼10% errors in the amplitude of the reconstructed wave packets visible in Figure 9 lead to only a ∼1% loss in fidelity may seem perplexing at first sight and deserves explanation. The resolution of this apparent conflict lies in the near-perfect reconstruction of the phase function shown in the same figure. Consider normalized target and reconstructed wave packets, $\psi_{tar}(x) = \alpha(x)\exp\{i\theta(x)\}$ and $\psi_{rec}(x) = [\alpha(x) + \delta(x)]\exp\{i\theta(x)\}$, respectively, with different amplitudes but the same spatial phase functions. Since both wave packets are normalized, it follows that $\int dx\alpha\delta = -{}^1/_2 \int dx\delta^2$. As a result, the amplitude error $\delta(x)$ affects the fidelity only in *second order*: $f = \int dx\psi_{tar}{}^*\psi_{rec} = 1 + \int dx\alpha\delta = 1 - (1/2)\int dx\delta^2$.

In the preceding examples of state reconstruction, our calculations of the fourth pulse propagator have relied on the actual dipole moment function for the E ← A electronic transition, a strongly coordinate-dependent function shown in Figure 10. But for many molecules—and especially for transitions involving at least one high-lying state—such detailed information is unavailable. We wish to investigate the extent to which reconstruction can be performed successfully using an approximate E ← A transition dipole function in calculating the pseudoinverse of the reference matrix. Assuming a linear form for $\mu_{EA}(R)$, we expand the transition dipole about the A-state equilibrium position. The resulting approximation is compared with the actual dipole function in Figure 10. With this linear approximation and the actual difference potential, we obtained a reconstructed state (not shown) of fidelity 0.9951

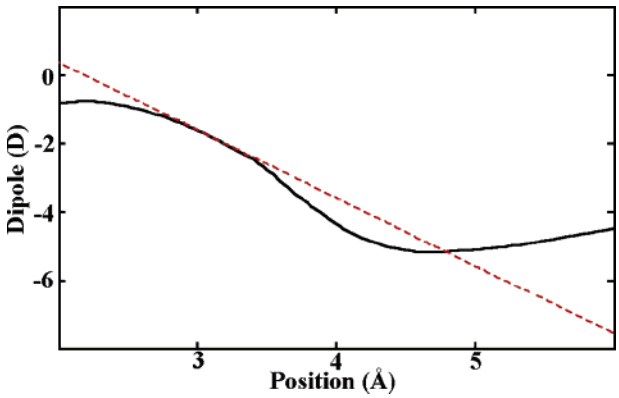

Figure 10. The actual E ← A transition dipole moment function (solid black line) and a linear approximation to it (dashed red line) given by $\mu_{EA} + \mu'_{EA}(R - R_A)$. The constants $\mu_{EA} = -1.798$ D and $\mu'_{EA} = -1.9811$ D/Å are the value and slope of the transition dipole at the A-state equilibrium position, $R_A = 3.09$ Å. In the important region between 2.5 and 5 Å, where the target-state amplitude is nonnegligible (see Figure 5), the mean relative error is 8%.

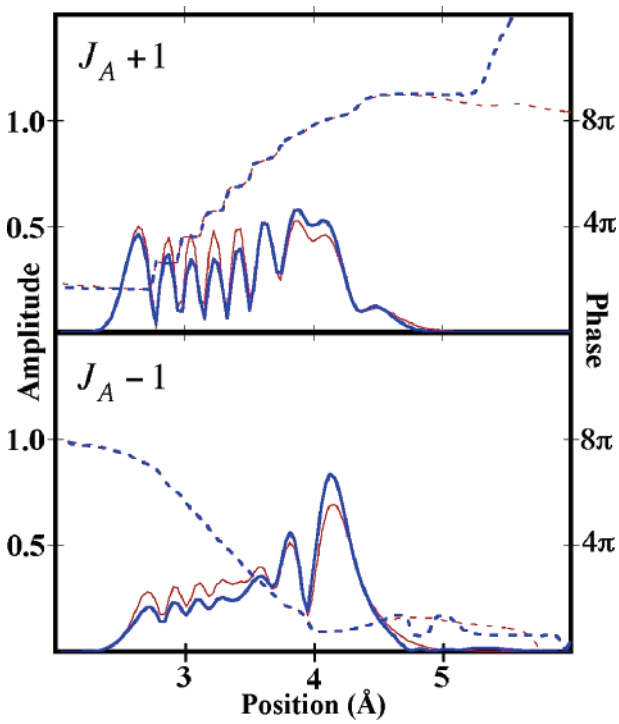

Figure 11. Same as Figure 8 but carrying out the reconstruction procedure with approximate reference states calculated by assuming both a constant difference potential between the A and E electronic levels and the linear approximation to the E ← A transition dipole moment function shown in Figure 10. The fidelity is 0.9831 with a tolerance of 0.0602.

(with tolerance 0.0474). This reconstruction is almost as accurate as that obtained with the actual dipole moment function.

We also carried out state reconstruction by combining the linear approximation to the transition dipole moment function with the constant approximation to the E ← A difference potential. As shown in Figure 11, from the rigorously calculated signal with 5% noise and the pseudoinverse of the doubly approximated reference matrix, we obtained a reconstructed state with fidelity 0.9831 (for a tolerance of 0.0602). Not surprisingly, this crudest approximation resulted in the lowest fidelity. But this reconstruction based on very rudimentary information about the potential function and transition-dipole moment function involving the final electronic state nonetheless yielded quite accurate wave packet components capturing the distinguishing features of the target state.

VI. Concluding Discussion

With rigorously calculated interferograms from a spectroscopically and theoretically well-characterized diatomic molecule, we have shown that two-color nonlinear WPI data will enable the direct reconstruction of time-evolved nuclear wave packets. The recovered dynamics is authentically multidimensional, as significant rotation−vibration couple precludes the separation of these degrees of freedom in the target E-state wave packet of Li_2.

Our results further predict that determination of the target wave packet with high fidelity can be achieved using only rudimentary information about the transition dipole moment function governing its preparation and the electronic potential curve on which it evolves. This feature supports the suggestion that nonlinear WPI holds promise as a tool for characterizing shaped nuclear wave packets generated on less-than-fully-characterized potential surfaces in quantum control experiments based on adaptive pulse shaping.

The proposed two-color nonlinear WPI experiments are a logical extension of earlier linear WPI experiments by Scherer and co-workers[24,25] and of our theoretical work on one-color nonlinear WPI.[39,41,43] In each case, the isolated interference signal is a time-dependent overlap between nuclear wave packets revealing amplitude-level information about their dynamics. We described nonlinear WPI signals generated with collinear phase-locked pulse pairs, detected by fluorescence (or some other action variable, such as photoionization or photodissociation, proportional to the population of a final electronic state) and isolated by optical phase cycling. But the proposed measurements could also be carried out using arrangements common to other existing applications of MDES.[1−15] Such measurements often use incident pulses in a noncollinear geometry and signal isolation by wave-vector matching. In those experiments, a third-order signal field carrying a record of third-order electronic coherence is heterodyne-detected by interference with an external local oscillator. In nonlinear WPI as described here, the relevant third-order coherence is converted into a fourth-order excited-state population by an internal local-oscillator pulse. Information obtained by both detection procedures is therefore essentially similar, but not strictly identical.[61] In contrast to wave-vector-matching methods, population detection by phase cycling is applicable in principle to nonextended samples such as single molecules or cells, and to turbid or optically dense media.

In many current applications of phase-sensitive MDES, interpulse delays and phase shifts are determined by spectral interferometry and may be passively maintained or prescribed by a diffractive-optics setup. The measurements required for wave packet reconstruction from nl-WPI data could be carried out using any of these arrangements. New techniques with specific advantages continue to be developed. A method of acousto-optical phase modulation, recently demonstrated by Tekavec and Marcus, deserves specific mention. Their approach to phase-sensitive electronic spectroscopy features both high sensitivity and a high signal-to-noise ratio.[62]

Although other multidimensional spectroscopies typically represent the signal in the frequency domain, our application of nonlinear WPI is most naturally formulated in a time-domain description. This approach facilitates interpretation of the interferogram in terms of wave packet overlaps, for example by using phase-space diagrams.[39,42,43] The time-domain repre-

sentation of the interferogram is also convenient for state reconstruction, as each signal point goes along with a single reference state specified by two interpulse delays.

Signal isolation by phase cycling, as summarized by eq 26, is familiar from NMR[63] and has recently been employed in ultrafast optical experiments by Warren and co-workers.[6] In that work, a phase-coherent pulse-pair produced a nonlinear polarization in an atomic system, and a delayed pulse converted the relevant portion of that polarization into an excited-state population. By varying the relative phases among these three pulses, Tian et al. used combinations of population measurements to isolate the photon echo signal, for example. A rudimentary application of optical phase cycling was made some time ago in the context of linear WPI.[25]

Neither the general treatment of nonlinear WPI in section II nor the molecular state reconstruction scheme in section III is specific to diatomic molecules. Some consideration has already been given to interference measurements of this kind in polyatomic molecules.[39] A recent theoretical study of intermolecular energy transfer[42] found that nonlinear WPI with polarized fields can provide amplitude-level information on the short-time vibrational dynamics accompanying and influencing coherent excitation transport.

Phase-sensitive fourth-order optical spectroscopies share the common feature that the molecular response is effectively linearized with respect to the incoming fields by detecting one or more quadrilinear signal components. The signal is therefore sensitive to quantum mechanical probability amplitudes rather than merely to probability densities. These measurements are sensitive *in first order* to the nuclear Hamiltonian that generates time evolution. Rearranging the time-dependent Schrödinger equation as

$$V(x) = \frac{1}{\psi(x,t)}\left[i\frac{\partial}{\partial t} - \frac{p^2}{2\mu}\right]\psi(x,t)$$

indicates how target states reconstructed from nonlinear WPI signals at a sequence of t_{43} values (together with finite-difference approximations for the kinetic energy operator and the time derivative) should enable direct reconstruction of the potential energy surface $V(x)$ along which wave packet motion proceeds. Preliminary calculations suggest that this means of excited-state potential determination could become a useful application of three-dimensional electronic spectroscopy.[64]

Acknowledgment. This paper is dedicated to Bob Silbey—former postdoctoral advisor to J.A.C.—whose insight, curiosity, guidance, and good humor are continuing sources of inspiration. This work was supported by grants from the US National Science Foundation and the donors of the Petroleum Research Fund administered by the American Chemical Society and by a J. S. Guggenheim Memorial Foundation Fellowship (to J.A.C.). Professor W. Meyer, University of Kaiserslautern, graciously provided us with tabulated information on the potential curves and transition dipole moment functions of Li_2. We thank Andy Marcus, Tom Dyke, and Patrick Tekavec for many helpful conversations on WPI and Stephen Leone and Elva Torres for specific guidance on ultrafast experiments in lithium.

Appendix

We can simplify the general expression (13) for the f-state amplitude by making use of the pulses' finite spectral bandwidth. Equations 3−5 and 12 allow the first-order operation of the jth pulse to be written as

$$-i\int_{-\infty}^{\infty} d\tau\, \langle f|\tilde{V}_j(\tau)|g\rangle = i\int_{-\infty}^{\infty} d\tau A_j(\tau - t_j)\cos\Phi_j(\tau - t_j)e^{iH_f(\tau-t_3)}\boldsymbol{\mu}_{fg}\cdot\mathbf{e}_j\, e^{-iH_g(\tau-t_3)} \cong e^{iH_f t_{j3}}P_j^{fg}e^{-iH_g t_{j3}} \quad \text{(A1)}$$

In arriving at the last member of eq A1, we made the rotating wave approximation and applied the definition (17) of the pulse propagator matrix elements for an upward electronic transition.

Denoting as $|n_a\rangle$ an eigenstate of H_a with energy $E_a(n_a)$ and referring to eq 6, we see that the individual vibronic elements of the first-order pulse propagator are proportional to Fourier components of the jth pulse

$$\langle n_f|P_j^{fg}|n_g\rangle = \frac{i}{2}\langle n_f|\boldsymbol{\mu}_{fg}\cdot\mathbf{e}_j|n_g\rangle\int_{-\infty}^{\infty} d\tau A_j(\tau)\times e^{-i\Phi_j(\tau)}e^{iE_f(n_f)\tau}e^{-iE_g(n_g)\tau} \quad \text{(A2)}$$

$$= i\langle n_f|\boldsymbol{\mu}_{fg}\cdot\mathbf{e}_j|n_g\rangle\alpha_j(E_f(n_f) - E_g(n_g))e^{-i\phi_j(E_f(n_f)-E_g(n_g))}$$

As a result of eq A2 and the finite bandwidths, only pulses 3 and 4 can generate f-state amplitude.

Because none of the pulses is resonant with the f ← e electronic transition, the process f ← e ← g cannot occur, and the second-order term in eq 13 makes no contribution to the f-state amplitude. Several third-order excitations can contribute though. The first arises from a member of the second pulse pair ($j = 3$ or 4) driving the sequence of transitions f ← g ← f ← g

$$i\int_{-\infty}^{\infty} d\tau\int_{-\infty}^{\tau} d\tau'\int_{-\infty}^{\tau'} d\tau''\langle f|\tilde{V}_j(\tau)|g\rangle\langle g|\tilde{V}_j(\tau')|f\rangle\langle f|\tilde{V}_j(\tau'')|g\rangle = e^{iH_f t_{j3}}R_j^{fg}e^{-iH_g t_{j3}} \quad \text{(A3)}$$

where electronic elements of the third-order pulse propagator are defined by

$$R_j^{fg} = \frac{-i}{8}\int_{-\infty}^{\infty} d\tau\int_{-\infty}^{\tau} d\tau'\int_{-\infty}^{\tau'} d\tau'' A_j(\tau)A_j(\tau')A_j(\tau'') e^{-i\Phi_j(\tau)+i\Phi_j(\tau')-i\Phi_j(\tau'')}e^{iH_f\tau}\boldsymbol{\mu}_{fg}\cdot\mathbf{e}_j e^{-iH_g(\tau-\tau')}\boldsymbol{\mu}_{gf}\cdot\mathbf{e}_j e^{-iH_f(\tau'-\tau'')}\boldsymbol{\mu}_{fg}\cdot\mathbf{e}_j e^{-iH_g\tau''} \quad \text{(A4)}$$

Both members of the second pulse-pair can work together to traverse the same f ← g ← f ← g sequence. As we are assuming $t_4 > t_3$ and neglecting effects due to pulse overlap, the relevant operators are

$$i\int_{-\infty}^{\infty} d\tau\int_{-\infty}^{\tau} d\tau'\int_{-\infty}^{\tau'} d\tau''\langle f|\tilde{V}_4(\tau)|g\rangle\langle g|\tilde{V}_3(\tau')|f\rangle\times\langle f|\tilde{V}_3(\tau'')|g\rangle = e^{iH_f t_{43}}P_4^{fg}e^{-iH_g t_{43}}Q_3^{gg} \quad \text{(A5)}$$

with

$$Q_3^{gg} = -\frac{1}{4}\int_{-\infty}^{\infty} d\tau'\int_{-\infty}^{\tau'} d\tau'' A_3(\tau')A_3(\tau'') e^{i\Phi_3(\tau')-i\Phi_3(\tau'')}e^{iH_g\tau'}\boldsymbol{\mu}_{gf}\cdot\mathbf{e}_3 e^{-iH_f(\tau'-\tau'')}\boldsymbol{\mu}_{fg}\cdot\mathbf{e}_3 e^{-iH_g\tau''} \quad \text{(A6)}$$

and

$$i\int_{-\infty}^{\infty} d\tau\int_{-\infty}^{\tau} d\tau'\int_{-\infty}^{\tau'} d\tau''\langle f|\tilde{V}_4(\tau)|g\rangle\langle g|\tilde{V}_4(\tau')|f\rangle\times\langle f|\tilde{V}_3(\tau'')|g\rangle = e^{iH_f t_{43}}Q_4^{ff}e^{-iH_f t_{43}}P_3^{fg} \quad \text{(A7)}$$

with

$$Q_4^{ff} = -\frac{1}{4}\int_{-\infty}^{\infty} d\tau\int_{-\infty}^{\tau} d\tau' A_4(\tau)A_4(\tau')e^{-i\Phi_4(\tau)+i\Phi_4(\tau')} e^{iH_f\tau}\boldsymbol{\mu}_{fg}\cdot\mathbf{e}_4 e^{-iH_g(\tau-\tau')}\boldsymbol{\mu}_{gf}\cdot\mathbf{e}_4 e^{-iH_f\tau'} \quad \text{(A8)}$$

Another third-order route to f-state amplitude is for a single member of the first pulse pair and a member of the second to drive the sequence f ← g ← e ← g. With $j = 3$, 4 and $k = 1$, 2, these transitions are effected by

$$i \int_{-\infty}^{\infty} d\tau \int_{-\infty}^{\tau} d\tau' \int_{-\infty}^{\tau'} d\tau'' \langle f|\tilde{V}_j(\tau)|g\rangle\langle g|\tilde{V}_k(\tau')|e\rangle \times \langle e|\tilde{V}_k(\tau'')|g\rangle = e^{iH_f t_{j3}} P_j^{fg} e^{-iH_g t_{jk}} Q_k^{gg} e^{-iH_g t_{k3}} \quad \text{(A9)}$$

where Q_k^{gg} is defined as in eq A6. Alternatively, both members of the first pulse pair can combine with a single pulse from the second pair to drive the same sequence

$$f \xleftarrow{j} g \xleftarrow{2} e \xleftarrow{1} g$$

where $j = 3,4$

$$i \int_{-\infty}^{\infty} d\tau \int_{-\infty}^{\tau} d\tau' \int_{-\infty}^{\tau'} d\tau'' \langle f|\tilde{V}_j(\tau)|g\rangle\langle g|\tilde{V}_2(\tau')|e\rangle \times \langle e|\tilde{V}_1(\tau'')|g\rangle = e^{iH_f t_{j3}} P_j^{fg} e^{-iH_g t_{j2}} P_2^{ge} e^{-iH_e t_{21}} P_1^{eg} e^{-iH_g t_{13}} \quad \text{(A10)}$$

Now we can evaluate the final-state amplitude. Multiplying eq 13 by $\exp\{-iH_f(t - t_3)\} = \exp\{-iH_f(t - t_4)\} \exp\{-iH_f t_{43}\}$ to revert to the Schrödinger picture, and making use of eqs A3, A5, A7, A9, and A10, we get

$$\begin{aligned}\langle f|\Psi(t \gg t_4)\rangle = e^{-iH_f(t-t_4)}\{&P_4^{fg} e^{-iH_g t_{43}} + e^{-iH_f t_{43}} P_3^{fg} + \\ &R_4^{fg} e^{-iH_g t_{43}} + e^{-iH_f t_{43}} R_3^{fg} + P_4^{fg} e^{-iH_g t_{43}} Q_3^{gg} + \\ &Q_4^{ff} e^{-iH_f t_{43}} P_3^{fg} + P_4^{fg} e^{-iH_g t_{42}} Q_2^{gg} e^{-iH_g t_{23}} + \\ &P_4^{fg} e^{-iH_g t_{41}} Q_1^{gg} e^{-iH_g t_{13}} + e^{-iH_f t_{43}} P_3^{fg} e^{-iH_g t_{32}} Q_2^{gg} e^{-iH_g t_{23}} + \\ &e^{-iH_f t_{43}} P_3^{fg} e^{-iH_g t_{31}} Q_1^{gg} e^{-iH_g t_{13}} + \\ &P_4^{fg} e^{-iH_g t_{42}} P_2^{ge} e^{-iH_e t_{21}} P_1^{eg} e^{-iH_g t_{13}} + \\ &e^{-iH_f t_{43}} P_3^{fg} e^{-iH_g t_{32}} P_2^{ge} e^{-iH_e t_{21}} P_1^{eg} e^{-iH_g t_{13}}\} |n_g\rangle \quad \text{(A11)}\end{aligned}$$

This expression provides explicit definitions for the 12 terms in eq 14 of section II.

References and Notes

(1) Cho, M.; Scherer, N. F.; Fleming, G. R.; Mukamel, S. *J. Chem. Phys.* **1992**, *96*, 5616.

(2) Mukamel, S. *Principles of Nonlinear Optical Spectroscopy*; Oxford University Press: New York, 1995.

(3) Warren, W. S.; Zewail, A. H. *J. Chem. Phys.* **1983**, *78*, 2279.

(4) Keusters, D.; Tan, H.-S.; Warren, W. S. *J. Phys. Chem. A* **1999**, *103*, 10369.

(5) Scheurer, C.; Mukamel, S. *J. Chem. Phys.* **2001**, *115*, 4989.

(6) Tian, P.; Keusters, D.; Suzaki, Y.; Warren, W. S. *Science* **2003**, *300*, 1553.

(7) Mukamel, S. *Ann. Rev. Phys. Chem.* **2000**, *51*, 691.

(8) Jonas, D. M. *Ann. Rev. Phys. Chem.* **2003**, *54*, 425.

(9) de Boeji, W. P.; Pshenichnikov, M. S.; Wiersma, D. A. *Chem. Phys.* **1998**, *233*, 287.

(10) Gallagher Faeder, S. M.; Jonas, D. M. *Phys. Rev. A* **2000**, *62*, 033820.

(11) Lepetit, L.; Joffre, M. *Opt. Lett.* **1996**, *21*, 564.

(12) Gallagher Faeder, S. M.; Albrecht, A. W.; Hybl, J. D.; Landin, B. L.; Rajaram, B.; Jonas, D. M. *J. Opt. Soc. Am. B* **1998**, *15*, 2338.

(13) Cowan, M. L.; Ogilvie, J. P.; Miller, R. J. D. *Chem. Phys. Lett.* **2004**, *386*, 184.

(14) Brixner, T.; Mančal, T.; Stiopkin, I. V.; Fleming, G. R. *J. Chem. Phys.* **2004**, *121*, 4221.

(15) Brixner, T.; Stenger, J.; Vaswani, H.; Cho, M.; Blankenship, R. E.; Fleming, G. R. *Nature* **2005**, *434*, 625.

(16) See the special issue on Quantum State Preparation and Measurement, Edited by W. P. Schleich and M. G. Raymer: *J. Mod. Opt.* **1998**, *44*, 11/12 and references therein.

(17) Assion, A.; Baumert, T.; Bergt, M.; Brixner, T.; Kiefer, B.; Zeyfried, V.; Strehle, M.; Gerber, G. *Science* **1998**, *282*, 919.

(18) Brixner, T.; Damrauer, N. H.; Niklaus, P.; Gerber, G. *Nature* **2001**, *414*, 57.

(19) Levis, R. J.; Menkir, G. M.; Rabitz, H. *Science* **2001**, *292*, 709.

(20) Herek, J. L.; Wohlleben, W.; Cogdell, R. J.; Zeidler, D.; Motzkus, M. *Nature* **2002**, *417*, 533.

(21) Judson, R. S.; Rabitz, H. *Phys. Rev. Lett.* **1992**, *68*, 1500.

(22) Rabitz, H.; de Vivie-Riedle, R.; Motzkus, M.; Kompa, K. *Science* **2000**, *288*, 824.

(23) Daniel, C.; Full, J.; González, L.; Lupulescu, C.; Manz, J.; Merli, A.; Vajada, Š.; Wöste, L. *Science* **2003**, *299*, 536.

(24) Scherer, N. F.; Carlson, R. J.; Matro, A.; Du, M.; Ruggiero, A. J.; Romero-Rochín, V.; Cina, J. A.; Fleming, G. R.; Rice, S. A. *J. Chem. Phys.* **1991**, *95*, 1487.

(25) Scherer, N. F.; Matro, A.; Ziegler, L. D.; Du, M.; Carlson, R. J.; Cina, J. A.; Fleming, G. R. *J. Chem. Phys.* **1992**, *96*, 4180.

(26) Metiu, H.; Engel, V. *J. Opt. Soc. Am. B* **1990**, *7*, 1709.

(27) Blanchet, V.; Nicole, C.; Bouchene, M. A.; Girard, B. *Phys. Rev. Lett.* **1997**, *78*, 2716.

(28) Bouchene, M. A.; Blanchet, V.; Nicole, C.; Melikechi, N.; Girard, B.; Ruppe, H.; Rutz, S.; Schreiber, E.; Wöste, L. *Eur. Phys. J. D* **1998**, *2*, 131.

(29) Bouchène, M. A.; Nicole, C.; Girard, B. *J. Phys. B* **1999**, *32*, 5167.

(30) Blanchet, V.; Bouchène, M. A.; Girard, B. *J. Chem. Phys.* **1998**, *108*, 4862.

(31) Ohmori, K.; Sato, Y.; Nikitin, E. E.; Rice, S. A. *Phys. Rev. Lett.* **2003**, *91*, 243003.

(32) Gühr, M.; Ibrahim, H.; Schwenter, N. *Phys. Chem. Chem. Phys.* **2004**, *6*, 5353.

(33) Milota, F.; Sperling, J.; Szöcs, V.; Tortschanoff, A.; Kauffmann, H. F. *J. Chem. Phys.* **2004**, *120*, 9870.

(34) Martínez-Galicia, R.; Romero-Rochín, V. *J. Chem. Phys.* **2005**, *122*, 094101.

(35) See: Heller, E. J. In *Advances in Classical Trajectory Methods*; Hase, W. L., Ed.; JAI Press: Greenwich, 1992; Vol. I, p 165.

(36) Leichtle, C.; Schleich, W. P.; Averbukh, I. Sh.; Shapiro, M. *Phys. Rev. Lett.* **1998**, *80*, 1418. Averbukh, I. Sh.; Shapiro, M.; Leichtle, C.; Schleich, W. P. *Phys. Rev. A* **1999**, *59*, 2163.

(37) Weinacht, T. C.; Ahn, J.; Bucksbaum, P. H. *Phys. Rev. Lett.* **1998**, *80*, 5508.

(38) Cina, J. A.; Harris, R. A. *J. Chem. Phys.* **1994**, *100*, 2531. Cina, J. A.; Harris, R. A. *Science* **1995**, *267*, 5199.

(39) Cina, J. A. *J. Chem. Phys.* **2000**, *113*, 9488.

(40) Duarte-Zamorano, R. P.; Romero-Rochín, V. *J. Chem. Phys.* **2001**, *114*, 9276.

(41) Cina, J. A.; Humble, T. S. *Bull. Chem. Soc. Jpn.* **2002**, *75*, 1135.

(42) Cina, J. A.; Kilin, D. S.; Humble, T. S. *J. Chem. Phys.* **2003**, *118*, 46.

(43) Humble, T. S.; Cina, J. A. *Bull. Korean Chem. Soc.* **2003**, *24*, 1111. *Bull. Korean Chem. Soc.* **2004**, *25*, 584.

(44) Ramos-Sánchez, S.; Romero-Rochín, V. *J. Chem. Phys.* **2004**, *121*, 2117.

(45) Humble, T. S.; Cina, J. A. *Phys. Rev. Lett.* **2004**, *93*, 060402.

(46) Schmidt-Mink, I.; Müller, W.; Meyer, W. *Chem. Phys.* **1985**, *92*, 263.

(47) Williams, R. M.; Papanikolas, J. M.; Rathje, J.; Leone, S. R. *J. Chem. Phys.* **1997**, *106*, 8310.

(48) Uberna, R.; Amitay, Z.; Loomis, R. A.; Leone, S. R. *Faraday Discuss.* **1999**, *113*, 385; Pesce, L.; Amitay, Z.; Uberna, R.; Leone, S.; Ratner, M.; Kosloff, R. *J. Chem. Phys.* **2001**, *114*, 1259.

(49) Stauffer, H. U.; Ballard, J. B.; Amitay, Z.; Leone, S. R. *J. Chem. Phys.* **2002**, *116*, 946.

(50) Amitay, Z.; Kosloff, R.; Leone, S. R. *Chem. Phys. Lett.* **2002**, *359*, 8.

(51) Ballard, J. B.; Arrowsmith, A. N.; Hüwel, L.; Dai, X.; Leone, S. R. *Phys. Rev. A* **2003**, *68*, 043409.

(52) Shen, Y.-C.; Cina, J. A. *J. Chem. Phys.* **1999**, *110*, 9793.

(53) By this statement, we mean specifically that in evaluating the amplitudes appearing in eq 14, the spectral phase of the second pulse obeys $\phi_2(\omega) = [\phi_2(\omega) - \phi_2(\omega_L)] + \phi_1(\omega_L) + \omega_L t_{21}$, in accordance with eq 7 for $\phi = 0$ (and analogously for $\phi_4(\omega)$, in accordance with eq 8 for $\phi' = 0$). Note that the quantity in square brackets is independent of the uncontrolled absolute phase of the second (or fourth) pulse.

(54) Tolstov, G. P. *Fourier Series*; Translated by R. A. Silverman; Dover: New York, 1976; Chapter 7.

(55) Leforestier, C.; et al. *J. Comput. Phys.* **1991**, *94*, 59.

(56) Press, W. H.; Teukolsky, S. A.; Vetterling, W. T.; Flannery, B. P. *Numerical Recipes in C*; Cambridge University Press: Cambridge, 1992.

(57) The numerical tolerance *T* is the inverse of the condition number; the latter is defined in ref 56.

(58) Goodisman, J. *Diatomic Interaction Potential Theory*; Loebel, E., Ed.; Academic Press: New York, 1973; Vol. 1.

(59) Gradshteyn, I. S.; Ryzhik, I. M. *Table of Integrals, Series, and Products*, 5th ed.; Jeffrey, A., Ed.; Academic Press: New York, 1994; p 2.

(60) McHale, Jeanne L. *Molecular Spectroscopy*; Prentice Hall, Upper Saddle River, NJ, 1999; Section 8.4.

(61) Albrecht, A. W.; Hybl, J. D.; Gallagher Faeder, S. M.; Jonas, D. M. *J. Chem. Phys.* **1999**, *111*, 10934. Erratum, *J. Chem. Phys.* **2001**, *115*, 5691.

(62) Tekavec, P.; Marcus, A. H. Private communication.

(63) Aue, A. P.; Bartholdi, E.; Ernst, R. R. *J. Chem. Phys.* **1976**, *64*, 2229.

(64) Dickson, N.; Humble, T. S.; Cina, J. A. Unpublished.